



# Optimizing dual-intermediates adsorption on Rh-based intermetallics for formic acid electrooxidation

Tao Shen<sup>a</sup>, Sijing Chen<sup>b</sup>, Shuang Wang<sup>a</sup>, Xiao Huang<sup>a</sup>, Min Song<sup>a</sup>, Xu Zhao<sup>a</sup>, Jingping Hu<sup>b</sup>, Deli Wang<sup>a,\*</sup>

<sup>a</sup> Key Laboratory of Material Chemistry for Energy Conversion and Storage (Huazhong University of Science and Technology), Ministry of Education, Hubei Key Laboratory of Material Chemistry and Service Failure, School of Chemistry and Chemical Engineering, Huazhong University of Science and Technology, Wuhan 430074, PR China

<sup>b</sup> School of Environmental Science and Engineering, Huazhong University of Science and Technology, Wuhan 430074, PR China

## ARTICLE INFO

### Keywords:

Fuel cells  
Electrocatalysis  
Formic acid oxidation reaction  
Rh-based nanoparticles  
Ordered intermetallics

## ABSTRACT

Concurrently optimizing the pathway and electrocatalytic activity for formic acid oxidation reaction (FAOR) is significant but still challenging. Herein, surface and composition engineering strategies are integrated by constructing atomically ordered Rh<sub>0.9</sub>Pt<sub>0.1</sub>Fe ternary intermetallic (O-Rh<sub>0.9</sub>Pt<sub>0.1</sub>Fe). Supported by the in situ infrared spectra, the carbon monoxide (CO\*) mediated indirect FAOR pathway on pure Rh is switched into a direct pathway on RhFe intermetallics (O-RhFe) with isolated Rh atoms, leading to a lower overpotential. Further composition engineering by forming O-Rh<sub>0.9</sub>Pt<sub>0.1</sub>Fe contributes to enhanced FAOR activity due to the stabilizing of COOH\* intermediate, as indicated by the density functional theory calculations. Besides, O-Rh<sub>0.9</sub>Pt<sub>0.1</sub>Fe shows enhanced FAOR activity during potential cycling tests with fewer structural evolutions, while O-RhFe displays a decay. This study provides new insight into tuning reaction pathways and catalytic activity selectively via tailoring adsorption of different intermediates.

## 1. Introduction

Direct formic acid fuel cell (DFAFC) has been considered as one of the promising portable electronic devices due to the high open circuit potential and low permeability of fuel through the membrane [1–3]. For the anodic formic acid oxidation reaction (FAOR), it could proceed via a direct pathway for the production of carbon dioxide (CO<sub>2</sub>) or an indirect pathway involving the adsorbed carbon monoxide (CO\*) as a poisoning intermediate [4–6]. However, the electrooxidation of CO\* into CO<sub>2</sub> relies on a higher overpotential [7], which greatly decreases the catalytic performances. Therefore, it is key to switch the FAOR pathway from an indirect pathway into the direct pathway through structure designing of electrocatalysts. Accordingly, how to promote the FAOR activity via the direct pathway simultaneously remains a new challenge.

Previous studies have shown that the adsorption of CO\* intermediate during FAOR is favored on the continuous Pt sites [8,9], which could be limited by isolating Pt atoms through surface decoration or forming alloys [10–13]. For example, hexagonal close-packed hollow and face-centred cubic hollow coordinated CO\* intermediates, which

occupy three Pt sites on pure Pt, displayed more negative adsorption energy than the apical and bridging coordinated CO\* intermediates on single sites and adjacent dual sites [9]. On the other hand, the binding of apical CO\* on Pt sites in single-atom alloys were much weaker than on pure Pt. As a consequence, Pt-based single-atom alloys or intermetallics with atomically dispersed Pt sites display enhanced FAOR activity than conventional Pt-based random alloys and pure Pt catalysts [14–19]. Similarly, isolating the Pd and Ir atomic sites could also enhance their FAOR activities by limiting the formation of the CO\*, which is present on the monometallic Pd and Ir catalysts [20–23]. Thus, isolating the active sites is a feasible strategy to improve the FAOR pathway selectivity. However, isolating the Pt-group metal atoms does not ensure an increased FAOR activity. N doped C anchored Ir single-atom catalysts (SACs) were highly efficient for FAOR, while Pt/Pd single-atom catalysts were almost inert [24], indicating the significant influence of coordination environments of isolated atoms. It is worth noting that the adsorption of other intermediates may also show an influence on the FAOR activity, the contribution of which is less concerned. The theoretical calculation revealed that isolated metal atoms coordinated with

\* Corresponding author.

E-mail address: [wangdl81125@hust.edu.cn](mailto:wangdl81125@hust.edu.cn) (D. Wang).

<https://doi.org/10.1016/j.apcatb.2023.122766>

Received 1 January 2023; Received in revised form 10 April 2023; Accepted 11 April 2023

Available online 12 April 2023

0926-3373/© 2023 Elsevier B.V. All rights reserved.

metals or N doped in carbon were favored on adsorption of different intermediates like COOH\* and HCOO\* [25]. For the direct FAOR pathway without CO\* formation, tuning the adsorption energy of COOH\* or HCOO\* via controlling the compositions of alloys is expected to optimize the FAOR performance. Thus, it is significant to optimize the adsorption energies of CO\*, HCOO\* and COOH\* simultaneously to promote FAOR catalytic performances in one catalyst. For the mono-metallic Pt-group metals, CO\* is overbinding while COOH\* and HCOO\* bind much more weakly than CO\* [26,27]. Thus, it is crucial to selectively reduce the binding of CO\* but increase the binding of COOH\* or HCOO\*.

Among Pt-group metals, Rh single atoms anchored by N-doped carbon exhibited superior activity towards FAOR compared with other single atom catalysts and nanoparticles due to the reduced binding of CO\* and favored adsorption of COOH\* and HCOO\* [28], which renders Rh as one of the most promising anodic electrocatalysts. In addition, doping or surface modifying with slight foreign metal atoms could result in a significant promoting effect due to the strain, ensemble or synergistic effect [29,30]. In this work, Rh-based intermetallics with isolated Rh atoms and tunable compositions are constructed to manipulate the intermediates adsorption properties of CO\* and COOH\* or HCOO\* for advancing the design of FAOR electrocatalysts. Binary Rh-based intermetallics were prepared first to analyze the influence of Rh ensemble size on the FAOR pathway by weakening the binding of CO\*. In situ attenuated infrared spectroscopy was employed to confirm that CO\* intermediate could be limited on Rh-based intermetallics. Then ternary Rh-based intermetallics were prepared to further explore the effect of COOH\* or HCOO\* adsorption on FAOR activity. Density functional theory (DFT) calculations were performed to validate the FAOR coordinates on different catalysts. Electrochemical dealloying treatment was performed to verify the merits of ternary intermetallics in promoting the FAOR stability relative to binary catalysts. Structural characterization results provide an insight into the relationship between the FAOR performances and reconstructed intermetallics after dealloying treatment. This work offers the opportunity to optimize the reaction selectivity and activity concurrently through engineering the atomic arrangement and composition of intermetallics.

## 2. Experimental procedures

### 2.1. Preparation of catalysts

The ordered RhFe, RhZn, and RhBi intermetallics were prepared via an impregnation-reduction method followed by the thermal treatment according to previous reported works [31]. Take the synthesis of ordered RhFe as an example. Firstly, 40.7 mg of RhCl<sub>3</sub>·3 H<sub>2</sub>O (0.194 mmol) and 31.5 mg of FeCl<sub>3</sub> (0.194 mmol) were dissolved in 6 mL of deionized water, and then 69.2 mg of Vulcan XC-72 carbon support was dispersed into the solution. The suspension was treated by ultrasound and heating at 55 °C alternatively until the water evaporate completely. After that, the obtained slurry was dried in a vacuum oven for 12 h and then ground into powder. Afterward, the powder was reduced in a tube furnace in 10% H<sub>2</sub>/Ar at 200 °C for 2 h. At last, 30 mg of pre-reduced samples were annealed at 700 °C for 4 h in 10% H<sub>2</sub>/Ar and the obtained samples were denoted as O-RhFe/C, where O means ordered intermetallic structure. Similarly, the carbon supported ordered RhZn (O-RhZn) and RhBi (O-RhBi) intermetallics were prepared with the same method except that the FeCl<sub>3</sub> was replaced by ZnCl<sub>2</sub> and BiCl<sub>3</sub>, respectively. To ensure a similar metal loading for binary intermetallics, the mass fraction of Rh in O-RhBi/C was decreased to 12% as Bi exhibits a higher atomic mass. Ternary Rh-based intermetallics including O-Rh<sub>0.9</sub>Pt<sub>0.1</sub>Fe, O-Rh<sub>0.9</sub>Ir<sub>0.1</sub>Fe and O-Rh<sub>0.9</sub>Ru<sub>0.1</sub>Fe were prepared with the same procedure with 10% of Rh was replaced by other Pt-group metals using H<sub>2</sub>PtCl<sub>6</sub>·6 H<sub>2</sub>O, IrCl<sub>3</sub>, and RuCl<sub>3</sub> precursors respectively. Rh/C was reduced at 200 °C in 10% H<sub>2</sub>/Ar for 2 h. Samples annealed at other temperatures for 3 h were named with a suffix of the value of

annealing temperature.

### 2.2. Physical characterization

The powder X-ray diffraction (XRD) of samples was measured by the X'Pert PRO diffractometer with a scan rate of 10°/min at 40 kV and 40 mA. The X-photoelectron spectra (XPS) were measured on an AXIS-ULTRA DLD-600 W equipment. The transmission electron microscopy (TEM) images were collected on a 200 keV field-emission S/TEM (FEI-Talos) equipped with four energy-dispersive X-ray detectors. The atomic resolution high angle annular dark field scanning transmission electron microscopy (HAADF-STEM) images are collected by the JEOL-NEOARM microscope. Thermal gravimetric (TG) was conducted by Pyris1 TGA instrument at a heating rate of 10 °C min<sup>-1</sup> in the Air atmosphere.

### 2.3. Electrochemical characterization

Electrochemical results were measured on PGSTAT302N Autolab electrochemical workstation equipped with a three-electrode electrolytic cell at 25 ± 2 °C. The glassy carbon electrode (0.196 cm<sup>2</sup>) coated by a catalyst layer, a carbon rod and a reverse hydrogen electrode (RHE) was selected as the working electrode, counter electrode and reference electrode, respectively. The working electrode was prepared by dropping 10 µL of the catalyst ink onto the glassy carbon and dried naturally, in which the catalysts ink was prepared by mixing 5 mg of samples with 1 mL of 0.1% Nafion/isopropanol solution. The electrocatalytic activity and stability were measured in N<sub>2</sub> saturated 0.5 M H<sub>2</sub>SO<sub>4</sub> solution containing 0.5 M HCOOH through cyclic voltammetry (CV), linear sweep voltammetry (LSV), and chronoamperometry (CA) methods. After the working electrode was held at 0.05 V for 10 min in CO saturated 0.5 M H<sub>2</sub>SO<sub>4</sub> and then N<sub>2</sub> was bubbled for 15 min to remove the residual CO, the CO stripping voltammetry was performed from 0.05 V to 1.2 V at 20 mV s<sup>-1</sup> with an initial potential at 0.05 V. Prior to the electrocatalytic tests, the working electrodes were immersed into 0.5 M H<sub>2</sub>SO<sub>4</sub> solution for 400 s and washed with ultrapure water to minimize the oxides on the surface of catalysts.

### 2.4. In situ attenuated total reflection infrared (ATR-IR) measurement

A detailed description of the ATR-IR setup equipped with an MCT detector and Si internal reflection element has been reported previously [21]. In brief, catalysts coated Si, Ti wire, and Ag/AgCl electrode were used as the working electrode, counter electrode and reference electrode respectively. The electrochemical spectral measurements were performed in 0.5 M H<sub>2</sub>SO<sub>4</sub> containing 0.5 M HCOOH and the spectra were collected at a resolution of 4 cm<sup>-1</sup> with 32 scans. The potential-resolved in situ ATR-IR spectra were collected from 0.05 to 1.2 V (vs. RHE) with an LSV scan rate at 1 mV s<sup>-1</sup>. The time-resolved in situ ATR-IR spectra were collected at 0.6 V (vs. RHE). The reference spectra were collected after the potential was held at 1.3 V for 1 min to remove the possible adsorbed species on electrodes.

## 3. Results and discussion

### 3.1. Preparation and characterization of electrocatalysts

The structural features of as-synthesized catalysts were probed by powder X-ray diffraction (XRD) technique. A broad diffraction peak at about 25° for Rh/C displayed in Fig. 1a was assigned to the (002) plane of the carbon support. Rh/C showed the face-centered cubic (fcc) polycrystalline structure with (111) as the dominant diffraction peak, in line with the standard card #01-087-0714. When binary RhFe intermetallics (O-RhFe/C) were formed, the crystalline phase transformed into a body-centered cubic (bcc) structure with (110) as the dominant diffraction peak. The super-lattice (100) of O-RhFe/C confirmed the ordered intermetallic structures, consistent with the standard card

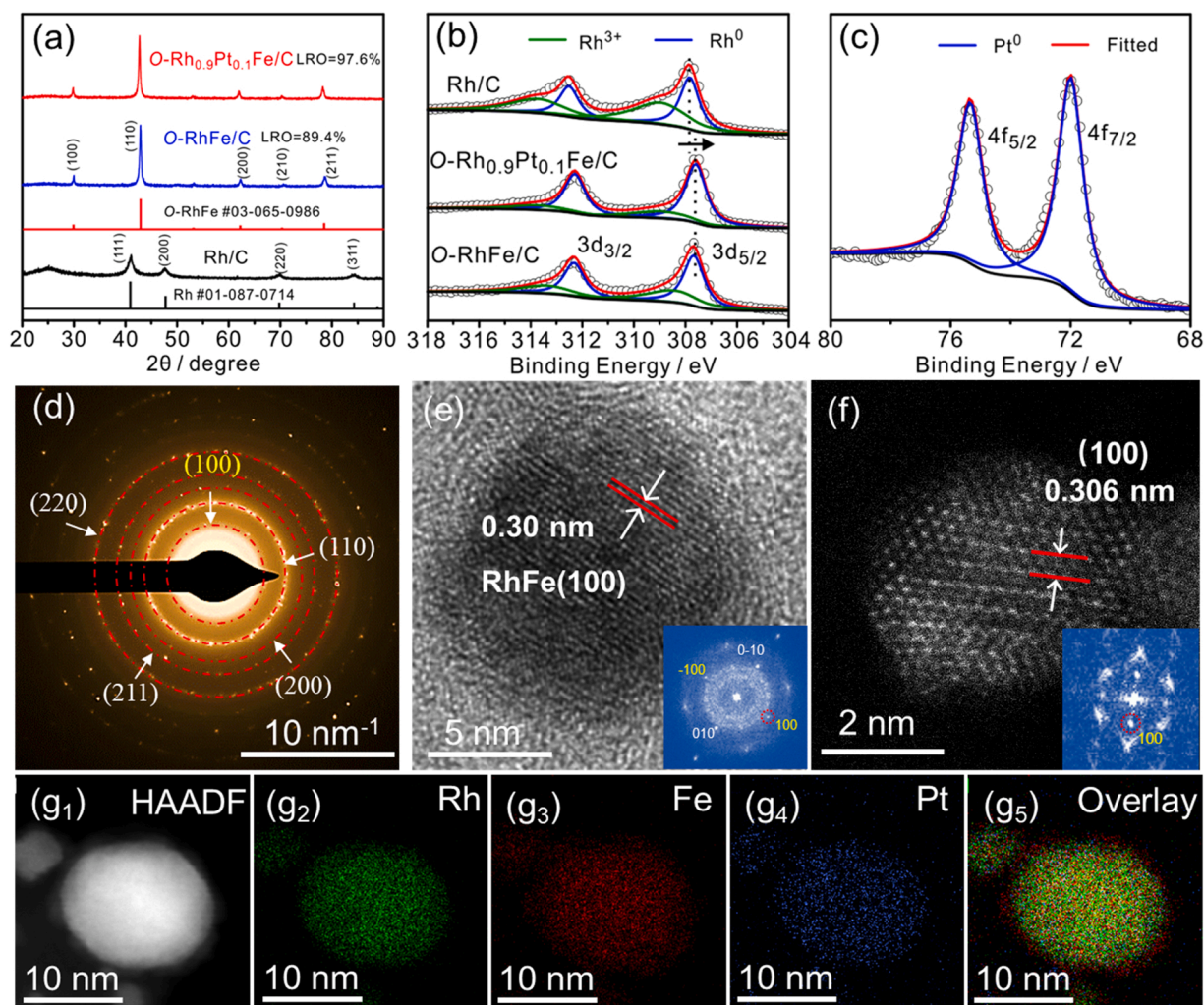


**Fig. 1.** (a) XRD patterns of Rh/C (black line), O-RhFe/C (blue line), O-Rh<sub>0.9</sub>Pt<sub>0.1</sub>Fe/C (red line) and the corresponding standard cards. (b) The fine XPS spectra for Rh 3d of Rh/C, O-RhFe/C and O-Rh<sub>0.9</sub>Pt<sub>0.1</sub>Fe/C. (c) The fine XPS spectrum for Pt 4 f of O-Rh<sub>0.9</sub>Pt<sub>0.1</sub>Fe/C. (d) The selected area electron diffraction (SAED) image of O-Rh<sub>0.9</sub>Pt<sub>0.1</sub>Fe/C. (e) High resolution transmission electron microscopy (HRTEM) and (f) atomic resolution scanning transmission electron microscope (STEM) image of O-Rh<sub>0.9</sub>Pt<sub>0.1</sub>Fe/C. The insets show the corresponding fast Fourier transform (FFT) images. (g<sub>1</sub>) High-angle annular dark field (HAADF) image of O-Rh<sub>0.9</sub>Pt<sub>0.1</sub>Fe/C and corresponding elemental maps of (g<sub>2</sub>) Rh, (g<sub>3</sub>) Fe, (g<sub>4</sub>) Pt and (g<sub>5</sub>) the overlay.

#03–065–0986. When 10% of Rh atoms in O-RhFe/C were replaced by Pt to form ternary intermetallic O-Rh<sub>0.9</sub>Pt<sub>0.1</sub>Fe/C, the ordered structure was well preserved according to the XRD patterns. Based on the XRD peak intensity ratio of super-lattice (100) and fundamental lattice (110) [32], the long-range ordering degrees (LRO) of O-Rh<sub>0.9</sub>Pt<sub>0.1</sub>Fe/C and O-RhFe/C were calculated to be 97.6% and 89.4%, respectively, indicating that Rh/Pt and Fe atoms were mainly atomically ordered distributed in nanoparticles.

The near-surface structural feature of electrocatalysts was analyzed via the X-photoelectron spectra (XPS). The fine XPS spectra of Rh 3d (Fig. 1b) were fitted into the metallic Rh (Rh<sup>0</sup>) and oxidized Rh (Rh<sup>3+</sup>). Rh/C displayed a higher content of Rh<sup>3+</sup> (55.8%) relative to O-RhFe/C (41.6%) due to its smaller average nanoparticle size, as the surface Rh atoms are easy to be oxidized in air [33]. The binding energy of Rh 3d for O-RhFe/C and O-Rh<sub>0.9</sub>Pt<sub>0.1</sub>Fe/C were close and shifted to a lower value relative to Rh/C, indicating that the electronic property of Rh was mainly tuned by Fe. The fine XPS spectrum of Pt 4 f (Fig. 1c) showed that metallic Pt was mainly present in O-Rh<sub>0.9</sub>Pt<sub>0.1</sub>Fe/C. The fine XPS spectra of Fe 2p (Fig. S1) of O-RhFe/C and O-Rh<sub>0.9</sub>Pt<sub>0.1</sub>Fe/C showed no obvious shift in binding energy, and the oxidized Fe species were mainly present on surfaces.

The selected area electron diffraction (SAED) image (Fig. 1d) also

indicates the formation of ordered ternary O-Rh<sub>0.9</sub>Pt<sub>0.1</sub>Fe/C intermetallics as revealed by the diffraction rings of (100) super-lattice and (110) lattice. In addition, the high-resolution transmission electron microscope (HRTEM) and atomic resolution scanning transmission electron microscope (STEM) images (Fig. 1e, f) displayed a lattice distance of about 0.30 nm, which is assigned to the (100) super-lattice. The corresponding fast Fourier transform (FFT) image further verifies the ordered intermetallic structure of O-Rh<sub>0.9</sub>Pt<sub>0.1</sub>Fe/C at nanoscale according to the diffraction spot of (100) super-lattice. As the atomic number of Pt or Rh is larger than that of Fe, the intensities of Pt and Rh atoms are stronger than that of Fe due to the Z contrast [29]. The dispersion of Pt atoms indicates that Pt has been doped into the lattice of RhFe intermetallics without surface segregation. The elemental maps (Fig. 1g) of Rh and Pt show similar distribution in the nanoparticle, while Fe shows a broader distribution as revealed in the overlay image, indicating that the surface of O-Rh<sub>0.9</sub>Pt<sub>0.1</sub>Fe nanoparticle was enriched with Fe or Fe oxides (Fig. S3c), in agreement with the XPS analysis. Besides, the TEM characterizations of binary O-RhFe/C (Fig. S2) confirmed its ordered structure, Fe or Fe oxides enriched surface and similar average nanoparticle size relative to O-Rh<sub>0.9</sub>Pt<sub>0.1</sub>Fe/C (Fig. S3).

For comparison, binary O-RhZn/C, O-RhBi/C, D-RhFe/C, and ternary O-Rh<sub>0.9</sub>Ru<sub>0.1</sub>Fe/C, O-Rh<sub>0.9</sub>Ir<sub>0.1</sub>Fe/C were prepared. The XRD patterns



(Fig. S4) and HRTEM images of O-RhZn/C (Fig. 2a) and O-RhBi/C (Fig. 2c) indicate their bcc and hexagonal close-packed (hcp) phases, respectively. The relevant research shows that the formation of ordered intermetallics from the salts precursors during thermal treatment is rely on the preformed alloys [34], although the phase transition from random alloy into the intermetallics could be happened under a milder temperature. As the reduction potential of Bi (+0.20 V from  $\text{Bi}^{3+}$ ) is higher than those of Fe (−0.04 V from  $\text{Fe}^{3+}$ ) and Zn (−0.76 V from  $\text{Zn}^{2+}$ ) and metallic Bi present a lower melting point (271 °C) than Zn (419 °C) and Fe (1535 °C), the inter-diffusion of Rh and Bi atoms is easier to form alloy than Rh and Fe or Zn atoms, followed by thermodynamically driven the phase transition from random alloy into the intermetallics. The (110) diffraction peaks of ternary Rh-based intermetallics shifted to a lower degree relative to that of O-RhFe/C (Figs. 2e and 2f), which was attributed to the differences in atomic radius ( $\text{Pt} > \text{Ir} > \text{Ru} = \text{Rh}$ ), leading to the lattice distortion at different degrees. The formation of Rh-based intermetallics was realized under a higher thermal treatment temperature (Fig. S4), which led to the increase in average nanoparticle size compared with Rh/C, as manifested by their TEM characterizations (Fig. S5–S7). However, O-RhZn/C displayed the Rh enriched surface (Fig. 2b) while O-RhBi/C showed no obvious surface segregation of specific elements (Fig. 2d), which was also reflected by the differences in adsorption of H (Fig. S10). The metal loadings of catalysts were calculated by the thermal gravimetric analysis (TGA) (Fig. S8). The calculated mass fractions of Rh in O-RhZn/C and O-RhBi/C are 21.0% and 12.6%, respectively. While the mass fraction of Rh in O-RhFe/C is about 44.3%, which may be due to the oxidation of carbon support catalyzed by  $\text{Fe}_2\text{O}_3$  during thermal treatment [35]. The metal loading of O-Rh<sub>0.9</sub>Ir<sub>0.1</sub>Fe/C is close to that of O-RhFe/C, indicating that Pt shows a minor influence on the loss of carbon.

### 3.2. Formic acid oxidation reaction (FAOR) performance

Electrochemical characterizations were employed to investigate the influence of structural features on electrocatalytic performances towards FAOR. Fig. 3a shows the linear sweep voltammetry (LSV) curves of Rh-based electrocatalysts in  $\text{N}_2$  saturated 0.5 M  $\text{H}_2\text{SO}_4$  containing 0.5 M  $\text{HCOOH}$  solution. It could be found that the onset potential for binary Rh-based intermetallics decreased significantly compared with that of Rh/C, indicating that  $\text{HCOOH}$  could be oxidized easily on ordered intermetallics. The measured apparent current density of Rh/C was higher than its real value due to the larger non-Faraday current, which was related to the surface area of catalysts. As shown in Fig. S9, all the binary Rh-based intermetallics showed enhanced FAOR activity compared with Rh/C at 0.4 V. O-RhFe/C exhibited the highest mass normalized activity (MA) both at 0.4 V and 0.7 V. The CO stripping curves could reflect the  $\text{CO}^*$  adsorption properties on different Rh-based catalysts. It could be seen that  $\text{CO}^*$  could be adsorbed on Rh/C, O-RhZn/C and O-RhBi/C, while it was suppressed on O-RhFe/C (Fig. S10a). The cyclic voltammetry (CV) curves of Rh/C, O-RhBi/C, O-RhZn/C and O-RhFe/C in 0.5 M  $\text{H}_2\text{SO}_4$  + 0.5 M  $\text{HCOOH}$  showed distinct behaviors in anodic (forward) and cathodic (backward) scanning directions (Fig. 3b–c and S10b–c). The ratio for peak current densities in forward and backward directions ( $j_f/j_b$ ) was employed to compare the selectivity via the direct pathway [36]. Among binary Rh-based intermetallics, the  $j_f/j_b$  value of O-RhFe/C is much larger than that of O-RhBi/C, O-RhZn/C and O-RhFe/C (Fig. S11), indicating a higher selectivity for the direct pathway.

In situ attenuated total reflection infrared (ATR-IR) combined with electrochemical tests was performed to monitor the intermediates during FAOR. A positive band at about  $2345\text{ cm}^{-1}$  is ascribed to the increment of  $\text{CO}_2$  relative to the reference spectrum. Two positive bands at about  $2010\text{ cm}^{-1}$  and  $1880\text{ cm}^{-1}$  (Fig. 3d) are ascribed to the

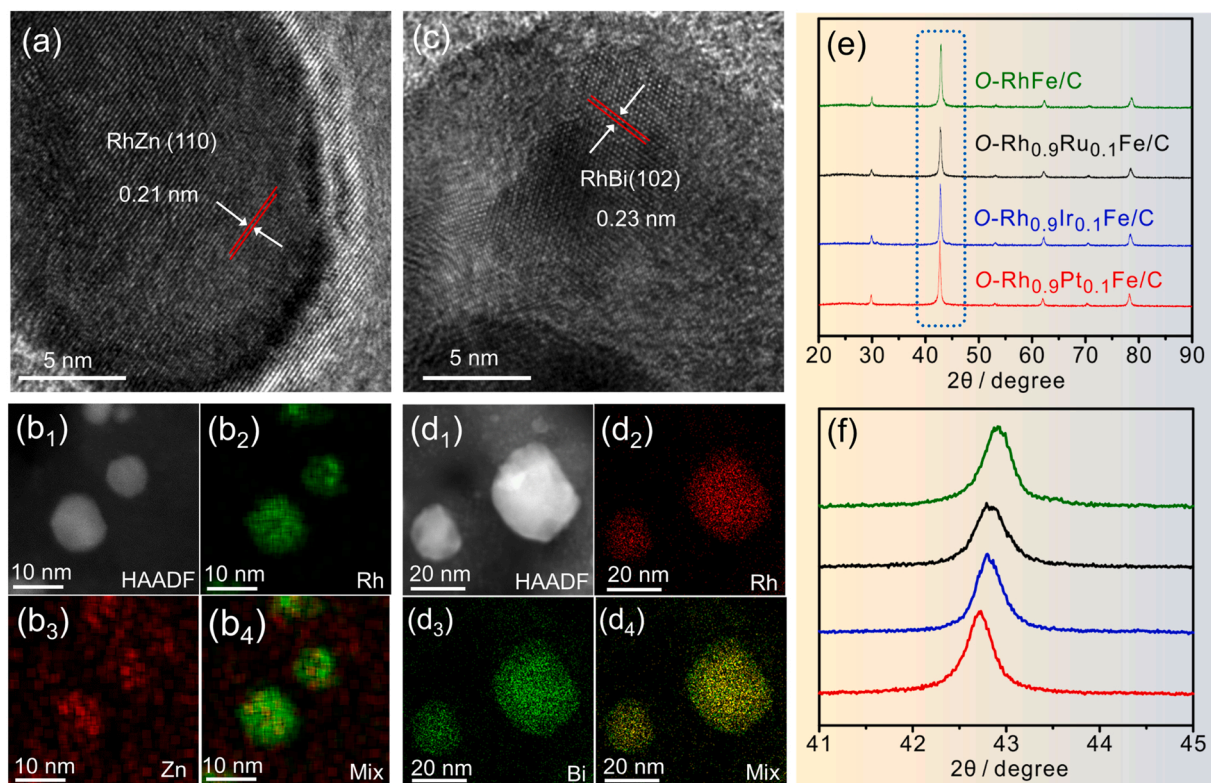


**Fig. 2.** (a) HRTEM images of O-RhZn nanoparticle. (b<sub>1</sub>) HAADF image of O-RhZn nanoparticles and corresponding elemental maps of (b<sub>2</sub>) Rh, (b<sub>3</sub>) Zn, and (b<sub>4</sub>) the composite of Rh and Zn. (c) HRTEM image of O-RhBi nanoparticle and (c) corresponding FFT image. (d<sub>1</sub>) HAADF image of O-RhBi nanoparticles and corresponding elemental maps of (d<sub>2</sub>) Rh, (d<sub>3</sub>) Bi, and (d<sub>4</sub>) the composite of Rh and Bi. (e) XRD patterns of O-RhFe/C, O-Rh<sub>0.9</sub>Ru<sub>0.1</sub>Fe/C, O-Rh<sub>0.9</sub>Ir<sub>0.1</sub>Fe/C and O-Rh<sub>0.9</sub>Pt<sub>0.1</sub>Fe/C. (f) The enlarged region in the box in (e).



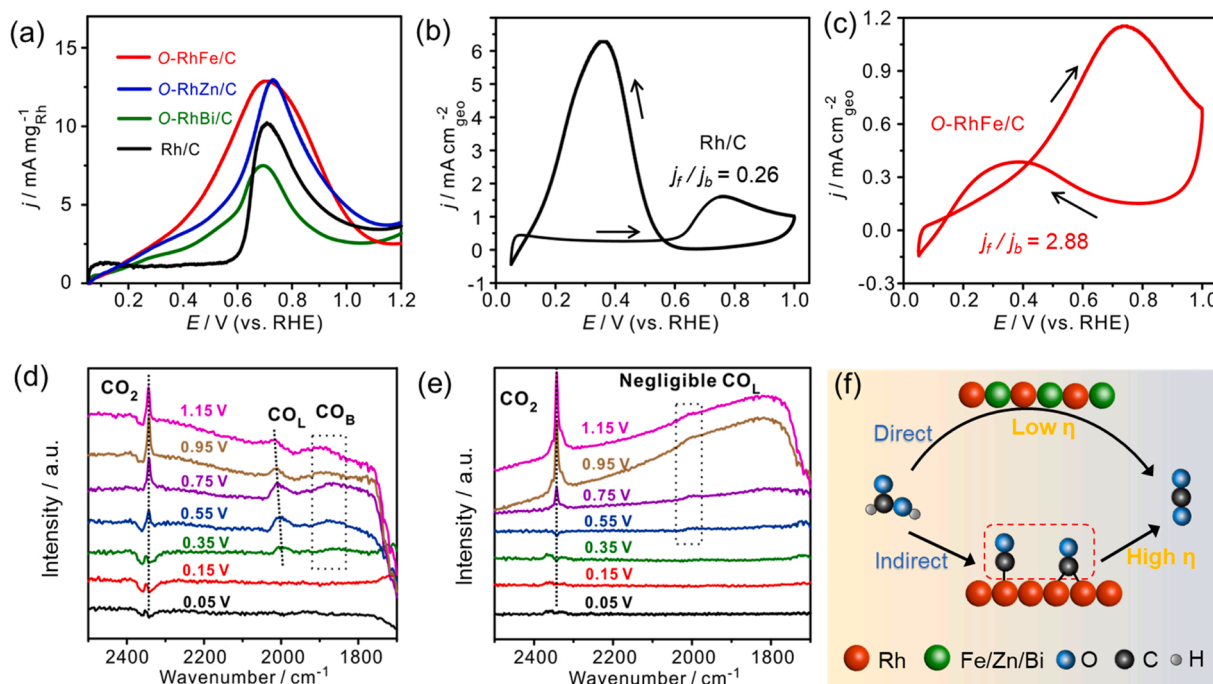


**Fig. 3.** (a) Linear sweep voltammetry (LSV) curves of Rh/C, O-RhBi/C, O-RhZn/C and O-RhFe/C in N<sub>2</sub> saturated 0.5 M H<sub>2</sub>SO<sub>4</sub> + 0.5 M HCOOH at 5 mV s<sup>-1</sup>. Cyclic voltammetry (CV) curves of (b) Rh/C and (c) O-RhFe/C in N<sub>2</sub> saturated 0.5 M H<sub>2</sub>SO<sub>4</sub> + 0.5 M HCOOH. Potential-resolved in situ ATR-IR spectra for FAOR on (d) Rh/C and (e) O-RhFe/C in N<sub>2</sub> saturated 0.5 M H<sub>2</sub>SO<sub>4</sub> + 0.5 M HCOOH. (f) Schematic diagram for the FAOR process on pure Rh and binary Rh-based intermetallics.

adsorbed CO\* on Rh surface with the linear (CO<sub>L</sub>) and bridged (CO<sub>B</sub>) conformation, respectively, consistent with previous reported results [37]. The shift of CO<sub>L</sub> band could be ascribed to the change in electrical field and charge transfer between electrode and CO<sub>L</sub> [37]. On the contrary, there is no obvious CO\* band on O-RhFe/C during FAOR (Fig. 3e). The time-resolved in situ ATR-IR spectra show that CO<sub>L</sub> forms firstly and

then CO<sub>B</sub> forms on Rh/C (Fig. S12a). However, even after 20 min, there is still no CO\* band on O-RhFe/C (Fig. S12b). It is easy to understand that the CO<sub>B</sub> could be inhibited by isolating the Rh atoms as two continuous Rh sites are required for the adsorption of CO<sub>B</sub>. While the results confirm that the adsorption of CO<sub>L</sub> is also greatly weakened on binary O-RhFe/C with atomically isolated Rh atoms. According to the in

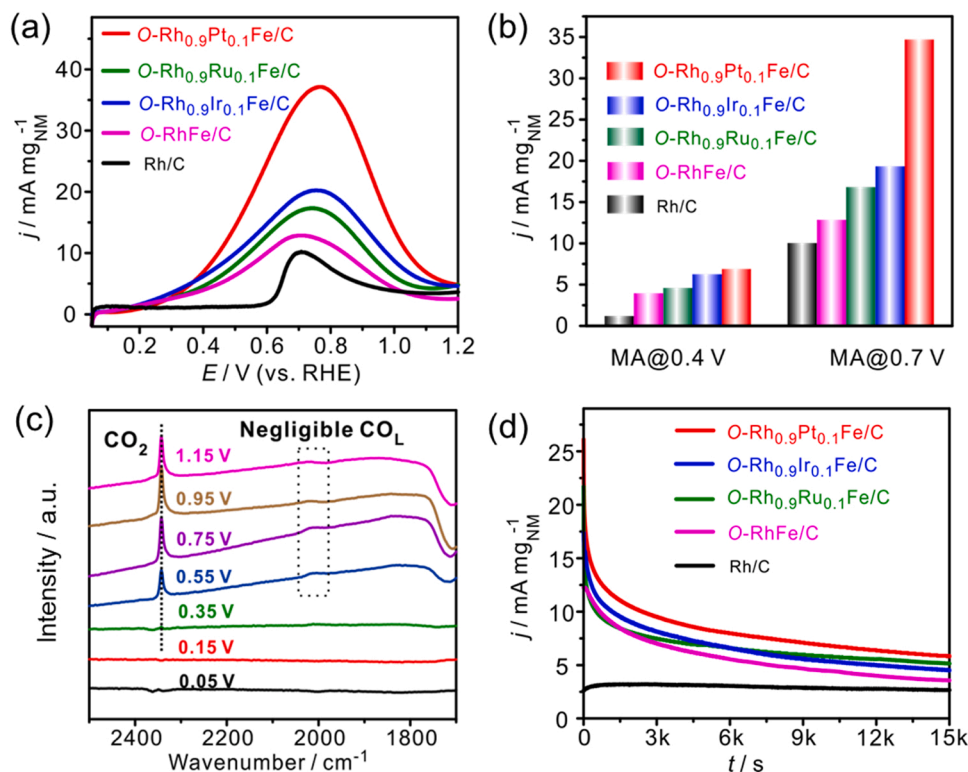


**Fig. 4.** (a) LSV curves and (b) noble metal mass normalized activity of Rh/C, O-RhFe/C, O-Rh<sub>0.9</sub>Pt<sub>0.1</sub>Fe/C, O-Rh<sub>0.9</sub>Ru<sub>0.1</sub>Fe/C, O-Rh<sub>0.9</sub>Ir<sub>0.1</sub>Fe/C and O-Rh<sub>0.9</sub>Pt<sub>0.1</sub>Fe/C in N<sub>2</sub> saturated 0.5 M H<sub>2</sub>SO<sub>4</sub> + 0.5 M HCOOH at 5 mV s<sup>-1</sup>. (c) Potential-resolved in situ ATR-IR spectra for FAOR on O-Rh<sub>0.9</sub>Pt<sub>0.1</sub>Fe/C in N<sub>2</sub> saturated 0.5 M H<sub>2</sub>SO<sub>4</sub> + 0.5 M HCOOH. (d) Chronoamperometric tests curves at 0.6 V of Rh/C, O-RhFe/C, O-Rh<sub>0.9</sub>Ru<sub>0.1</sub>Fe/C, O-Rh<sub>0.9</sub>Ir<sub>0.1</sub>Fe/C and O-Rh<sub>0.9</sub>Pt<sub>0.1</sub>Fe/C in N<sub>2</sub> saturated 0.5 M H<sub>2</sub>SO<sub>4</sub> + 0.5 M HCOOH.

situ ATR-IR and electrocatalytic results, constructing Rh-based intermetallics is effective to promote the FAOR selectivity via the direct pathway by limiting the formation of CO\* intermediates (Fig. 3f).

Ternary Rh-based intermetallics were prepared for further regulating the adsorption of intermediates on Rh. As shown in Fig. 4a, all ternary intermetallics showed decreased FAOR onset potentials compared with Rh/C and enhanced activity compared with O-RhFe/C. O-Rh<sub>0.9</sub>Pt<sub>0.1</sub>Fe/C (Fig. 4b) showed the highest FAOR activity both at a lower overpotential (0.4 V) and a higher overpotential (0.7 V) relative to O-Rh<sub>0.9</sub>Ir<sub>0.1</sub>Fe/C and O-Rh<sub>0.9</sub>Ru<sub>0.1</sub>Fe/C. Besides, all the ternary Rh-based intermetallics exhibited limited CO\* adsorption and their  $j_f/j_b$  values were larger than 1 (Fig. S13), indicating the weaker binding of CO\* intermediates. The potential-resolved in situ ATR-IR spectra (Fig. 4c) further confirmed that FAOR proceeded mainly via the direct pathway on O-Rh<sub>0.9</sub>Pt<sub>0.1</sub>Fe/C. Although monometallic Pt nanoparticles also favored the formation of CO\* during FAOR [9], the IR results showed that both the Rh and Pt could be tolerant to CO\* poisoning by forming ternary intermetallics. In the meantime, ternary intermetallics also exhibited higher current densities during the chronoamperometric tests (Fig. 4d).

### 3.3. Density functional theory (DFT) calculation

DFT calculations were performed to uncover the FAOR mechanisms on different Rh-based electrocatalysts. The detailed methods for DFT was described in the Supplementary Information. According to previously reported works on FAOR, adsorbed CO\* worked as the intermediate during the indirect pathway while HCOO\* and COOH\* worked as the intermediates during the direct pathway [16,27]. In addition, COOH\* worked as the precursor for both CO\* and CO<sub>2</sub>. In this work, Rh (111), O-RhFe(110) and O-Rh<sub>0.9</sub>Pt<sub>0.1</sub>Fe(110) (Fig. 5a-c) were selected as they were the most thermally stable facets to exposing for face centered cubic and body centered cubic materials [38]. The adsorption

configurations of CO\*, COOH\* and HCOO\* on Rh(111), O-RhFe(110) and O-Rh<sub>0.9</sub>Pt<sub>0.1</sub>Fe(110) were displayed in Fig. S14-S16.

As shown in Fig. 5d-f, the adsorption of COOH\* was preferred than HCOO\* intermediate with a more negative free energy on the three catalysts. Then the COOH\* was favored on dissociation into CO\* rather than CO<sub>2</sub> on Rh (Fig. 5d). Thus, FAOR is easy to proceed with an indirect pathway on pure Rh according to the calculation results, consistent with the IR results. When forming O-RhFe intermetallics, the adsorption of COOH\* was still preferred than HCOO\*. However, the CO\* intermediate became thermally unfavorable than CO<sub>2</sub> (Fig. 5e), indicating the direct FAOR pathway on binary RhFe intermetallics. Similarly, FAOR also tended to proceed with the direct pathway on ternary O-Rh<sub>0.9</sub>Pt<sub>0.1</sub>Fe. Nevertheless, the more negative free energy of COOH\* on O-Rh<sub>0.9</sub>Pt<sub>0.1</sub>Fe than on O-RhFe suggested a decreased energy barrier for the FAOR (Fig. 5f), which was corresponding to the enhanced FAOR activity. As shown in Fig. 5g, both the bridged CO\* and atop CO\* displayed much more negative free energy on Rh than on O-RhFe and O-Rh<sub>0.9</sub>Pt<sub>0.1</sub>Fe, indicating that isolating the Rh atoms was beneficial for limiting the poisoning of CO\* intermediate. On the other hand, both COOH\* and HCOO\* were stabilized as the formation of binary and ternary intermetallics. Thus, both the FAOR activity and direct pathway were optimized via forming ternary intermetallics. For the reported Rh single atom catalysts, both the binding of COOH\* and HCOO\* were enhanced as well as the reduced binding of CO\*. Besides, two steps involving the dissociation of HCOOH into HCOO\* and HCOO\* into CO<sub>2</sub> were both thermodynamically favourable [28], which suggested the superior FAOR activity than the metallic catalysts. Therefore, isolating the Rh atoms could limit the binding of CO\* while tailoring the adsorption of COOH\* or HCOO\* is crucial for increasing the FAOR activity.

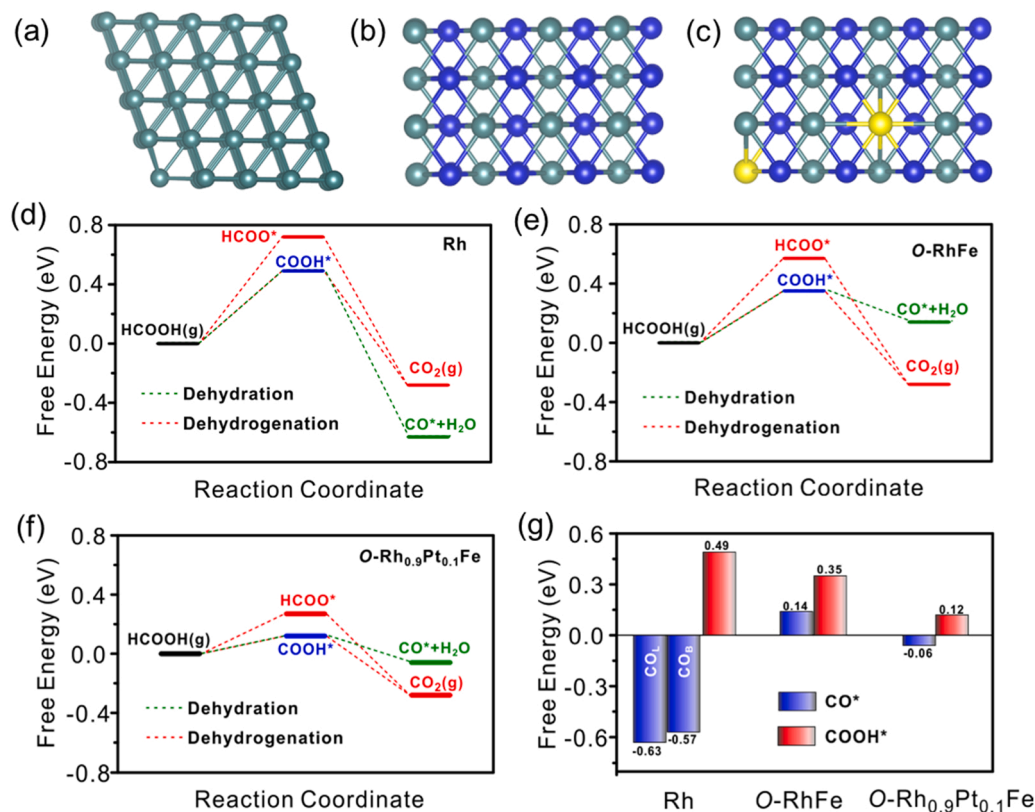


**Fig. 5.** Optimized slab models for the most stable facets of (a) Rh(111), (b) O-RhFe(110) and (c) O-Rh<sub>0.9</sub>Pt<sub>0.1</sub>Fe(110). The cyan, blue and yellow balls represent the Rh atom, Fe atom and Pt atom respectively. FAOR coordinate via the dehydration (indirect) and dehydrogenation (direct) pathway on (d) Rh(111), (e) O-RhFe(110) and (f) O-Rh<sub>0.9</sub>Pt<sub>0.1</sub>Fe(110). (g) Calculated free energies of CO\* and COOH\* on the Rh(111), O-RhFe(110) and O-Rh<sub>0.9</sub>Pt<sub>0.1</sub>Fe(110).

### 3.4. Stability tests

The stability of O-Rh<sub>0.9</sub>Pt<sub>0.1</sub>Fe/C was evaluated via a potential cycling in the potential ranges between 0.05 V and 1.0 V. It can be seen that after 100 cycles, both the O-RhFe/C and O-Rh<sub>0.9</sub>Pt<sub>0.1</sub>Fe/C (Fig. 6a and b) showed increased hydrogen adsorption/desorption regions, indicating a transformation of Fe/FeO<sub>x</sub> enriched surface into the Rh/Pt enriched surface. The FAOR current density of O-RhFe/C during the anodic scanning increased below 0.3 V after potential cycling (Fig. 6c), which was caused by the overlay of non-Faraday current due to H desorption. When catalyzing FAOR, O-RhFe/C showed a decreased peak current density about 50% after potential cycling. In contrast, O-Rh<sub>0.9</sub>Pt<sub>0.1</sub>Fe/C showed a 2.4 times promotion in peak current density after potential cycling with a slight decrease at lower potentials (Fig. 6d). For both catalysts, their  $j_f/j_b$  values decreased after potential cycling (Fig. S17), indicating increased CO\* binding strength. Therefore, the performance variations are determined by the integral effect in the adsorption property for CO\* and COOH\* after potential cycling. According to the DFT results, the differences for FAOR activity change of O-RhFe/C and O-Rh<sub>0.9</sub>Pt<sub>0.1</sub>Fe/C are proposed in Fig. 6e. For binary O-RhFe/C after potential cycling, the formation of larger Rh atomic ensembles would favor the binding of CO\* and decrease the binding of COOH\*, leading to the decreased FAOR activity. In contrast, the content of Pt on surface increased and might further optimize the adsorption of COOH\* for ternary O-Rh<sub>0.9</sub>Pt<sub>0.1</sub>Fe/C even though the binding of CO\* was promoted, contributing to a further increased FAOR activity after potential cycling.

### 3.5. Structural characterization after stability test

To further uncover the reason for the greatly improved FAOR stability in ternary O-Rh<sub>0.9</sub>Pt<sub>0.1</sub>Fe/C relative to binary O-RhFe/C, the phase, average particle size and composition of both catalysts after potential cycling were probed by TEM. As shown in the SAED images (Fig. 7a), the diffraction ring corresponding to (100) super-lattice was detected on O-Rh<sub>0.9</sub>Pt<sub>0.1</sub>Fe/C but less pronounced on O-RhFe/C. The HRTEM images of O-RhFe/C (Fig. S19a) and O-Rh<sub>0.9</sub>Pt<sub>0.1</sub>Fe/C (Fig. S20a) after potential cycling showed that their body-centered cubic

crystal phases were preserved as indicated by the lattice distance of (100), which was absent on the face-centered cubic Rh. O-Rh<sub>0.9</sub>Pt<sub>0.1</sub>Fe nanoparticles displayed a decrease in average particle size from 6.8 nm to 5.1 nm (Fig. 7b and S18a), while the average particle size of O-RhFe nanoparticles decreased from 6.4 nm to 4.3 nm after potential cycling (Fig. 7c and S18b). The less loss in average particle size for O-Rh<sub>0.9</sub>Pt<sub>0.1</sub>Fe maybe attributed to that Pt is more resistant to corrosion than Rh in acid medium [39]. These results manifested that the structural stability was enhanced when forming ternary intermetallics. As the surface composition mainly influences the FAOR selectivity, it is significant to reduce the larger Rh/Pt atomic ensembles during the reaction process. As shown in Fig. 7d, the elemental maps of O-RhFe nanoparticle showed a Rh enriched surface feature after potential cycling, which was favored for the adsorption of CO\* intermediates, resulting in decreased FAOR activity. However, the elemental maps of O-Rh<sub>0.9</sub>Pt<sub>0.1</sub>Fe nanoparticle (Fig. 7e) showed that both Rh and Pt were enriched on the surface, which was beneficial for the preservation of smaller Rh and Pt ensembles. The additional HAADF images and elemental maps further confirmed the formation of Rh shell and Pt/Rh shell on O-RhFe/C (Fig. S19b-e) and O-Rh<sub>0.9</sub>Pt<sub>0.1</sub>Fe/C (Fig. S20b-f) respectively after potential cycling. Thus, Pt not only tailored the adsorption properties of RhFe, but also contributed to the improved structural stability, confirming the superiority of ternary intermetallics relative to binary counterpart.

## 4. Conclusion

In summary, surface and composition engineering strategies have been integrated to enhance the FAOR performance of Rh-based electrocatalysts. Decreasing the Rh ensemble size into isolated Rh atoms by surface engineering, the FAOR activity is increased gradually, which is ascribed to limited formation of CO\* intermediate. When FAOR proceeds via the direct pathway, the activity could be enhanced by stabilizing COOH\* through tuning the compositions of Rh-based intermetallics according to the DFT calculations. Pt in ternary O-Rh<sub>0.9</sub>Pt<sub>0.1</sub>Fe/C plays a significant role in promoting stability by enhancing COOH\* adsorption and limiting larger Rh ensembles relative to binary O-RhFe. These results are beneficial for guiding the design of

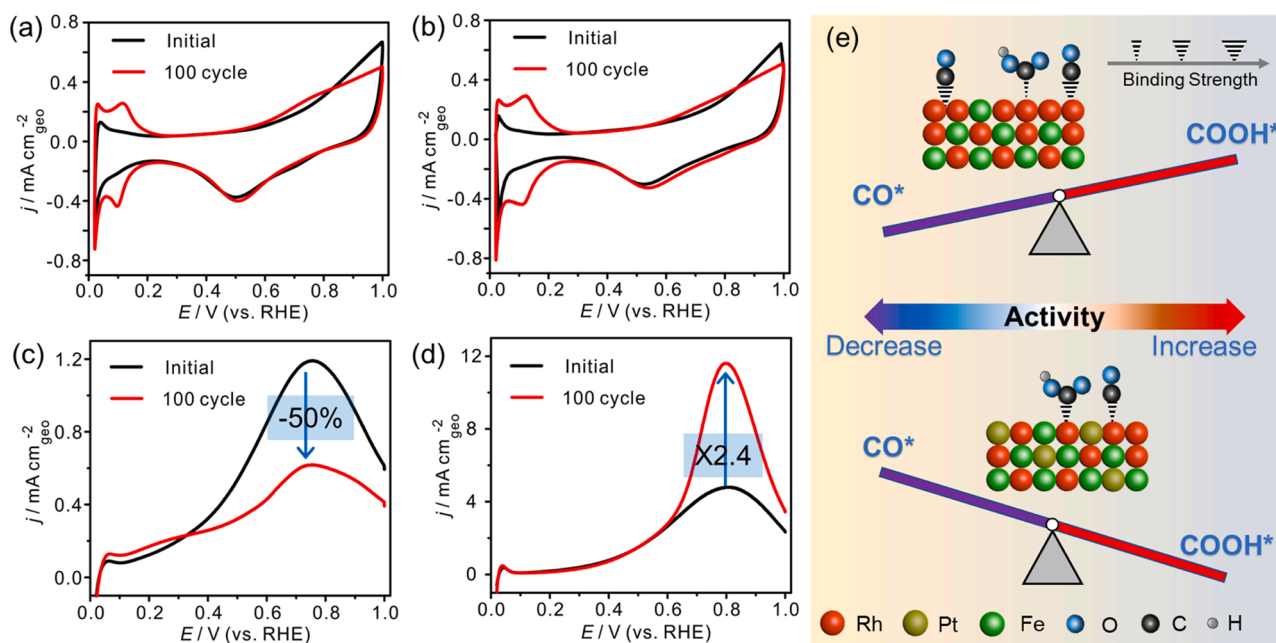


**Fig. 6.** CV curves of (a) O-RhFe/C and (b) O-Rh<sub>0.9</sub>Pt<sub>0.1</sub>Fe/C before and after potential cycling for 100 cycles in N<sub>2</sub>-saturated 0.5 M H<sub>2</sub>SO<sub>4</sub>. CV curves of (c) O-RhFe/C and (d) O-Rh<sub>0.9</sub>Pt<sub>0.1</sub>Fe/C before and after potential cycling for 100 cycles in N<sub>2</sub>-saturated 0.5 M H<sub>2</sub>SO<sub>4</sub> + 0.5 M HCOOH during the anodic scanning. (e) Schematic illustration for the influences of COOH\* and CO\* on FAOR activity for O-RhFe/C and O-Rh<sub>0.9</sub>Pt<sub>0.1</sub>Fe/C after potential cycling.



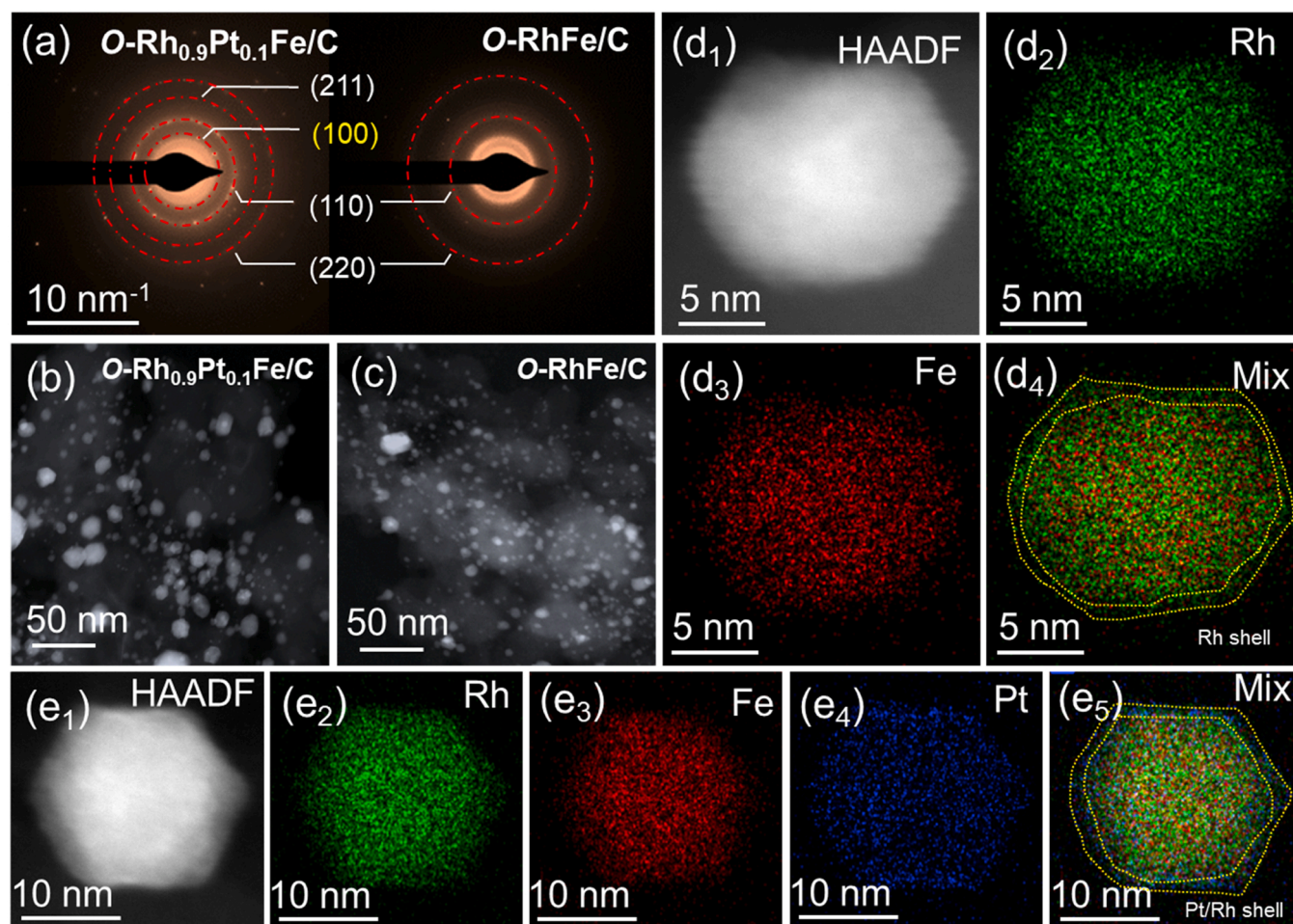


**Fig. 7.** (a) The SAED images of O-Rh<sub>0.9</sub>Pt<sub>0.1</sub>Fe/C (left) and O-RhFe/C (right) after potential cycling for 100 cycles. STEM images of (b) O-Rh<sub>0.9</sub>Pt<sub>0.1</sub>Fe/C and (c) O-RhFe/C after potential cycling. (d<sub>1</sub>) HAADF image of O-RhFe nanoparticle after potential cycling and corresponding elemental maps of (d<sub>2</sub>) Rh, (d<sub>3</sub>) Fe and (d<sub>4</sub>) the composite of Rh and Fe. (e<sub>1</sub>) HAADF image of O-Rh<sub>0.9</sub>Pt<sub>0.1</sub>Fe nanoparticle after potential cycling and corresponding elemental maps of (e<sub>2</sub>) Rh, (e<sub>3</sub>) Fe, (e<sub>4</sub>) Pt and (e<sub>5</sub>) the composite of Rh, Fe and Pt.

highly active FAOR electrocatalysts by tuning the adsorption properties of dual intermediates. This work confirms ternary intermetallics are promising electrocatalysts that could further optimize the catalytic performances and enhance the stability.

#### CRediT authorship contribution statement

**Tao Shen:** Conceptualization, Investigation, Methodology, Data curation, Writing – original draft. **Sijing Chen:** Methodology, Formal analysis, Data curation. **Shuang Wang:** Data curation, Writing – review & editing. **Xiao Huang:** Data curation, Formal analysis. **Min Song:** Data curation, Writing – review & editing. **Xu Zhao:** Writing – review & editing. **Jingping Hu:** Writing – review & editing. **Deli Wang:** Conceptualization, Project administration, Supervision, Writing – review & editing, Funding acquisition.

#### Declaration of Competing Interest

The authors declare that they have no known competing financial interests or personal relationships that could have appeared to influence the work reported in this paper.

#### Data availability

Data will be made available on request.

#### Acknowledgments

This work was supported by the National Natural Science Foundation of China (91963109) and the Innovation Research Funds of Huazhong University of Science and Technology (2172019kfyRCPY100). We thank the Analytical and Testing Center of Huazhong University of Science & Technology for allowing us to use its facilities for XRD, XPS and TEM measurements.

#### Appendix A. Supporting information

Supplementary data associated with this article can be found in the online version at [doi:10.1016/j.apcatb.2023.122766](https://doi.org/10.1016/j.apcatb.2023.122766).

#### References

- [1] R. Bhaskaran, B.G. Abraham, R. Chetty, Recent advances in electrocatalysts, mechanism, and cell architecture for direct formic acid fuel cells, *WIREs Energy Environ.* 11 (2021), e419, <https://doi.org/10.1002/wene.419>.
- [2] U.B. Demirci, Thermodynamic and environmental concerns, *J. Power Sources* 169 (2007) 239–246, <https://doi.org/10.1016/j.jpowsour.2007.03.050>.
- [3] X. Yu, P.G. Pickup, Recent advances in direct formic acid fuel cells (DFAFC), *J. Power Sources* 182 (2008) 124–132, <https://doi.org/10.1016/j.jpowsour.2008.03.075>.
- [4] A. Capon, R. Parsons, The oxidation of formic acid at noble metal electrodes Part III. Intermediates and mechanism on platinum electrodes, *J. Electroanal. Chem. Interfacial Electrochem.* 45 (1973) 205–231, [https://doi.org/10.1016/S0022-0728\(73\)80158-5](https://doi.org/10.1016/S0022-0728(73)80158-5).

- [5] Y.X. Chen, M. Heinen, Z. Jusys, R.J. Behm, Kinetics and mechanism of the electrooxidation of formic acid—spectroelectrochemical studies in a flow cell, *Angew. Chem. Int. Ed.* 45 (2006) 981–985, <https://doi.org/10.1002/anie.200502172>.
- [6] A. Cuesta, G. Cabello, M. Osawa, C. Gutiérrez, Mechanism of the electrocatalytic oxidation of formic acid on metals, *ACS Catal.* 2 (2012) 728–738, <https://doi.org/10.1021/cs200661z>.
- [7] V. Celorrio, P.M. Quaino, E. Santos, J. Flórez-Montañó, J.J.L. Humphrey, O. Guillén-Villafuerte, D. Plana, M.J. Lázaro, E. Pastor, D.J. Fermín, Strain effects on the oxidation of CO and HCOOH on Au–Pd core–shell nanoparticles, *ACS Catal.* 7 (2017) 1673–1680, <https://doi.org/10.1021/acscatal.6b03237>.
- [8] W. Zhong, Y. Qi, M. Deng, The ensemble effect of formic acid oxidation on platinum–gold electrode studied by first-principles calculations, *J. Power Sources* 278 (2015) 203–212, <https://doi.org/10.1016/j.jpowsour.2014.12.071>.
- [9] P.N. Duchesne, Z.Y. Li, C.P. Deming, V. Fung, X. Zhao, J. Yuan, T. Regier, A. Aldalbahi, Z. Almarhoon, S. Chen, D.E. Jiang, N. Zheng, P. Zhang, Golden single-atomic-site platinum electrocatalysts, *Nat. Mater.* 17 (2018) 1033–1039, <https://doi.org/10.1038/s41563-018-0167-5>.
- [10] X. Bi, R. Wang, Y. Ding, Boosting the performance of Pt electro-catalysts toward formic acid electro-oxidation by depositing sub-monolayer Au clusters, *Electrochim. Acta* 56 (2011) 10039–10043, <https://doi.org/10.1016/j.electacta.2011.08.101>.
- [11] Y.-X. Wang, C.-F. Liu, M.-L. Yang, X.-H. Zhao, Z.-X. Xue, Y.-Z. Xia, Concave Pt–Cu–Fe ternary nanocubes: One-pot synthesis and their electrocatalytic activity of methanol and formic acid oxidation, *Chin. Chem. Lett.* 28 (2017) 60–64, <https://doi.org/10.1016/j.ccllet.2016.05.025>.
- [12] Y.-X. Wang, T.-H. Chen, A high dispersed Pt<sub>0.35</sub>Pd<sub>0.35</sub>Co<sub>0.30</sub>/C as superior catalyst for methanol and formic acid electro-oxidation, *Chin. Chem. Lett.* 25 (2014) 907–911, <https://doi.org/10.1016/j.ccllet.2014.04.031>.
- [13] T.-J. Gan, J.-P. Wu, S. Liu, W.-J. Ou, B. Ling, X.-W. Kang, Low-crystallinity and heterostructured AuPt–Ru@CNTs as highly efficient multifunctional electrocatalyst, *J. Electrochem.* 28 (2022) 2201241.
- [14] E. Casado-Rivera, D.J. Volpe, L. Alden, C. Lind, C. Downie, T. Vázquez-Alvarez, A. C.D. Angelo, F.J. DiSalvo, H.D. Abruna, Electrocatalytic activity of ordered intermetallic phases for fuel cell applications, *J. Am. Chem. Soc.* 126 (2004) 4043–4049, <https://doi.org/10.1021/ja038497a>.
- [15] X. Ji, K.T. Lee, R. Holden, L. Zhang, J. Zhang, G.A. Botton, M. Couillard, L.F. Nazar, Nanocrystalline intermetallics on mesoporous carbon for direct formic acid fuel cell anodes, *Nat. Chem.* 2 (2010) 286–293, <https://doi.org/10.1038/nchem.553>.
- [16] S. Luo, W. Chen, Y. Cheng, X. Song, Q. Wu, L. Li, X. Wu, T. Wu, M. Li, Q. Yang, K. Deng, Z. Quan, Trimetallic synergy in intermetallic PtSnBi nanoplates boosts formic acid oxidation, *Adv. Mater.* 31 (2019), e1903683, <https://doi.org/10.1002/adma.201903683>.
- [17] M. Liu, Z. Liu, M. Xie, Z. Zhang, S. Zhang, T. Cheng, C. Gao, Ligand-mediated self-terminating growth of single-atom Pt on Au nanocrystals for improved formic acid oxidation activity, *Adv. Energy Mater.* 12 (2021) 2103195, <https://doi.org/10.1002/aenm.202103195>.
- [18] J. Kim, C.-W. Roh, S.K. Sahoo, S. Yang, J. Bae, J.W. Han, H. Lee, Highly durable platinum single-atom alloy catalyst for electrochemical reactions, *Adv. Energy Mater.* 8 (2018) 1701476, <https://doi.org/10.1002/aenm.201701476>.
- [19] Y. Kang, L. Qi, M. Li, R.E. Diaz, D. Su, R.R. Adzic, E. Stach, J. Li, C.B. Murray, Highly Active Pt<sub>3</sub>Pb and Core–Shell Pt<sub>3</sub>Pb–Pt Electrocatalysts for Formic Acid Oxidation, *ACS Nano* 6 (2012) 2818–2825, <https://doi.org/10.1021/nn3003373>.
- [20] T. Shen, S. Chen, R. Zeng, M. Gong, T. Zhao, Y. Lu, X. Liu, D. Xiao, Y. Yang, J. Hu, D. Wang, H.L. Xin, H.D. Abruna, Tailoring the antipoisoning performance of Pd for formic acid electrooxidation via an ordered PdBi intermetallic, *ACS Catal.* 10 (2020) 9977–9985, <https://doi.org/10.1021/acscatal.0c01537>.
- [21] T. Shen, S. Chen, C. Zhang, Y. Hu, E. Ma, Y. Yang, J. Hu, D. Wang, Engineering Ir atomic configuration for switching the pathway of formic acid electrooxidation reaction, *Adv. Funct. Mater.* 32 (2021) 2107672, <https://doi.org/10.1002/adfm.202107672>.
- [22] M.M. Flores Espinosa, T. Cheng, M. Xu, L. Abatemarco, C. Choi, X. Pan, W. A. Goddard, Z. Zhao, Y. Huang, Compressed Intermetallic PdCu for Enhanced Electrocatalysis, *ACS Energy Lett.* 5 (2020) 3672–3680, <https://doi.org/10.1021/acseenergylett.0c01959>.
- [23] T. Gunji, S.H. Noh, T. Tanabe, B. Han, C.Y. Nien, T. Ohsaka, F. Matsumoto, Enhanced electrocatalytic activity of carbon-supported ordered intermetallic palladium–lead (Pd<sub>3</sub>Pb) nanoparticles toward electrooxidation of formic acid, *Chem. Mater.* 29 (2017) 2906–2913, <https://doi.org/10.1021/acs.chemmater.6b05191>.
- [24] Z. Li, Y. Chen, S. Ji, Y. Tang, W. Chen, A. Li, J. Zhao, Y. Xiong, Y. Wu, Y. Gong, T. Yao, W. Liu, L. Zheng, J. Dong, Y. Wang, Z. Zhuang, W. Xing, C.T. He, C. Peng, W.C. Cheong, Q. Li, M. Zhang, Z. Chen, N. Fu, X. Gao, W. Zhu, J. Wan, J. Zhang, L. Gu, S. Wei, P. Hu, J. Luo, J. Li, C. Chen, Q. Peng, X. Duan, Y. Huang, X.M. Chen, D. Wang, Y. Li, Iridium single-atom catalyst on nitrogen-doped carbon for formic acid oxidation synthesized using a general host-guest strategy, *Nat. Chem.* 12 (2020) 764–772, <https://doi.org/10.1038/s41557-020-0473-9>.
- [25] A. Bagger, K.D. Jensen, M. Rashedi, R. Luo, J. Du, D. Zhang, L.J. Pereira, M. Escudero-Escribano, M. Arenz, J. Rossmeisl, Correlations between experiments and simulations for formic acid oxidation, *Chem. Sci.* 13 (2022) 13409–13417, <https://doi.org/10.1039/d2sc05160e>.
- [26] A.O. Elnabawy, J.A. Herron, J. Scaranto, M. Mavrikakis, Structure sensitivity of formic acid electrooxidation on transition metal surfaces: a first-principles study, *J. Electrochem. Soc.* 165 (2018) J3109–J3121, <https://doi.org/10.1149/2.0161815jes>.
- [27] A.O. Elnabawy, E.A. Murray, M. Mavrikakis, Trends in formic acid electro-oxidation on transition metals alloyed with platinum and palladium, *J. Phys. Chem. C* 126 (2022) 4374–4390, <https://doi.org/10.1021/acs.jpcc.1c10488>.
- [28] Y. Xiong, J. Dong, Z.Q. Huang, P. Xin, W. Chen, Y. Wang, Z. Li, Z. Jin, W. Xing, Z. Zhuang, J. Ye, X. Wei, R. Cao, L. Gu, S. Sun, L. Zhuang, X. Chen, H. Yang, C. Chen, Q. Peng, C.R. Chang, D. Wang, Y. Li, Single-atom Rh/N-doped carbon electrocatalyst for formic acid oxidation, *Nat. Nanotechnol.* 15 (2020) 390–397, <https://doi.org/10.1038/s41565-020-0665-x>.
- [29] S. Luo, L. Zhang, Y. Liao, L. Li, Q. Yang, X. Wu, X. Wu, D. He, C. He, W. Chen, Q. Wu, M. Li, E.J.M. Hensen, Z. Quan, A. Tensile-Strained Pt–Rh Single-Atom Alloy, Remarkably boosts ethanol oxidation, *Adv. Mater.* 33 (2021), e2008508, <https://doi.org/10.1002/adma.202008508>.
- [30] M. Tang, W. Chen, S. Luo, X. Wu, X. Fan, Y. Liao, X. Song, Y. Cheng, L. Li, L. Tan, Y. Liu, Z. Quan, Trace Pd modified intermetallic PtBi nanoplates towards efficient formic acid electrocatalysis, *J. Mater. Chem. A* 9 (2021) 9602–9608, <https://doi.org/10.1039/d1ta01123e>.
- [31] D. Wang, H.L. Xin, R. Hovden, H. Wang, Y. Yu, D.A. Muller, F.J. DiSalvo, H. D. Abruna, Structurally ordered intermetallic platinum–cobalt core–shell nanoparticles with enhanced activity and stability as oxygen reduction electrocatalysts, *Nat. Mater.* 12 (2013) 81–87, <https://doi.org/10.1038/nmat3458>.
- [32] D. Kim, C. Xie, N. Becknell, Y. Yu, M. Karamad, K. Chan, E.J. Crumlin, J. K. Norskov, P. Yang, Electrochemical activation of CO<sub>2</sub> through atomic ordering transformations of AuCu nanoparticles, *J. Am. Chem. Soc.* 139 (2017) 8329–8336, <https://doi.org/10.1021/jacs.7b03516>.
- [33] J. Zhang, J. Ye, Q. Fan, Y. Jiang, Y. Zhu, H. Li, Z. Cao, Q. Kuang, J. Cheng, J. Zheng, Z. Xie, Cyclic penta-twinned rhodium nanobranes as superior catalysts for ethanol electro-oxidation, *J. Am. Chem. Soc.* 140 (2018) 11232–11240, <https://doi.org/10.1021/jacs.8b03080>.
- [34] W.J. Zeng, C. Wang, Q.Q. Yan, P. Yin, L. Tong, H.W. Liang, Phase diagrams guide synthesis of highly ordered intermetallic electrocatalysts: separating alloying and ordering stages, *Nat. Commun.* 13 (2022) 7654, <https://doi.org/10.1038/s41467-022-35457-1>.
- [35] X. Gong, Z. Guo, Z. Wang, Variation on anthracite combustion efficiency with CeO<sub>2</sub> and Fe<sub>2</sub>O<sub>3</sub> addition by Differential Thermal Analysis (DTA), *Energy* 35 (2010) 506–511, <https://doi.org/10.1016/j.energy.2009.10.017>.
- [36] G.C. Luque, M.A. Montero, M.R. Gennero de Chialvo, A.C. Chialvo, Study of the formic acid electrooxidation on rhodium on steady state using a flow cell: potential dependence of the CO coverage, *Electrocatalysis* 11 (2020) 405–412, <https://doi.org/10.1007/s12678-020-00599-7>.
- [37] Q. Xu, I.V. Pobelov, T. Wandlowski, A. Kuzume, ATR-SEIRAS study of formic acid adsorption and oxidation on Rh modified Au(111–25 nm) film electrodes in 0.1 M H<sub>2</sub>SO<sub>4</sub>, *J. Electroanal. Chem.* 793 (2017) 70–76, <https://doi.org/10.1016/j.jelechem.2016.09.049>.
- [38] M. Chen, G. Gupta, C.W. Ordóñez, A.R. Lamkins, C.J. Ward, C.A. Abolafia, B. Zhang, L.T. Rolling, W. Huang, Intermetallic nanocatalyst for highly active heterogeneous hydroformylation, *J. Am. Chem. Soc.* 143 (2021) 20907–20915, <https://doi.org/10.1021/jacs.1c09665>.
- [39] M. Łukaszewski, A. Czerwiński, Anodic oxidation of Pd alloys with Pt and Rh, *J. Alloy. Compd.* 473 (2009) 220–226, <https://doi.org/10.1016/j.jallcom.2008.05.037>.